Supplementary Information for:

On-chip sampling of optical fields with attosecond resolution

Mina R. Bionta[1,†,*], Felix Ritzkowsky[2,†,*], Marco Turchetti[1,†], Yujia Yang[1], Dario Cattozzo Mor[1], William P. Putnam[3], Franz X. Kärtner[2], Karl K. Berggren[1], and Phillip D. Keathley[1,*]

[1] *Research Laboratory of Electronics, Massachusetts Institute of Technology, 77 Massachusetts Avenue, Cambridge, MA 02139, USA*

[2] *Deutsches Elektronen Synchrotron (DESY) & Center for Free-Electron Laser Science, Notkestraße 85, 22607 Hamburg, Germany*

[3] *Department of Electrical and Computer Engineering, University of California, Davis, 1 Shields Ave, Davis, CA 95616, USA*

[†] *These authors contributed equally to this work.*

[*] *e-mail: mbionta@mit.edu; felix.ritzkowsky@desy.de; pdkeat2@mit.edu*

S1. Experimental Setup

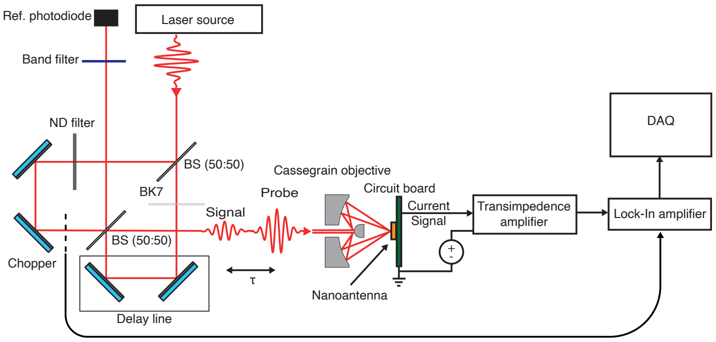

Figure S1. **Experimental Setup** Overview of the optical layout and signal detection chain of our experiments. Abbreviations: BS: beamsplitter, ND: neutral density filter, DAQ: data acquisition.

A CEP-stable, 78 MHz Er:fiber-based supercontinuum laser source was used, with a central wavelength of ∼1170 nm and pulse duration of ∼10 fs FWHM. A dispersion-balanced Mach-Zehnder interferometer was used to generate the pulse pairs for the experiment (Fig. S1). An Inconel reflective neutral density (ND) filter of optical density (OD) 4 on a 2 mm thick BK7 substrate (Thorlabs) was placed in one arm and used to generate a weak signal pulse with pulse energy of ∼5 fJ. An optical chopper was placed in this weak arm for lock-in amplification and detection. The strong, driver arm had a pulse energy of ∼50 pJ. A corresponding 2 mm thick BK7 window was placed in the driver arm to balance the dispersion between arms. The added chirp from the glass was precompensated using the prism compressor. The delay between the two pulses was controlled with a home built 15 μm piezo stage. The generated electron emission is collected and amplified by a transimpedance amplifier (FEMTO Messtechnik GmbH). The resulting voltage signal is demodulated by the Lock-In amplifier with the 200 Hz frequency of the chopper wheel and subsequently low-pass filtered.

S2. Discussion of Sampling Bandwidth

A strong local electric-field transient (driver) drives the electron emission at the metallic nanoantenna[1–4]. For simplicity in this section we will be discussing the field driving the emission at a surface, $E_{\mathrm{D}}(t)$. When a weak electric-field waveform (signal) perturbs the emission process, the detected time-averaged current is proportional to the electric field of the small signal. The small-signal gain, as defined by $\frac{\mathrm{d}\Gamma}{\mathrm{d}E}\big|_{E_{\mathrm{D}}(t)}$, is therefore dictated by the strong driving electric field waveform. To demonstrate the influence of the FWHM of the driving pulse duration on the sampling bandwidth, we calculated $\tilde{H}_{\mathrm{Det}}(\omega)$ for 1-, 3-, 5-, 7-, and 9-cycle sech^2 driver pulses each with a central frequency of 250 THz and a peak field strength at the antenna surface of 15 GV m^{-1} (see Fig. S2a).

The small-signal gain $\frac{\mathrm{d}\Gamma}{\mathrm{d}E}\big|_{E_{\mathrm{D}}(t)}$ was calculated by assuming Fowler-Nordheim tunneling emission with a characteristic tunneling field of $F_t = 78.7$ V nm^{-1}. Fig. S2b shows the effective gate signal $\frac{\mathrm{d}\Gamma}{\mathrm{d}E}\big|_{E_{\mathrm{D}}(t)}$ for the sampling process for each pulse duration. Only the single-cycle pulse (blue) exhibits an isolated peak. However, for driver pulses with an increasing number of cycles, satellite pulses start to emerge. For the 9-cycle case (green traces) the height of satellite pulses at -4 fs and 4 fs approach the height of the center peak. Fig. S2c shows the Fourier transform of $\frac{\mathrm{d}\Gamma}{\mathrm{d}E}\big|_{E_{\mathrm{D}}(t)}$.

The sampling bandwidth generated by a single-cycle field transient (Fig. 2C, blue curve) shows a smooth response from DC to 1.8 PHz and corresponds to the Fourier transform of the isolated peak in Fig. S2b (blue trace). With increasing pulse duration, the bandwidth becomes increasingly modulated due to the destructive interference of the additional peaks in the gate signal. The modulation is periodic with the frequency f_0 of the driving electric field at 250 THz and exhibits maxima at the higher harmonics $n \cdot f_0$ for $n\ \varepsilon\ \mathbb{N}$. We highlight that although a 5-cycle driver waveform results in strong modulation of the sampling response $\tilde{H}_{\mathrm{Det}}(\omega)$, the sampling response does not completely vanish at the minima (yellow traces). However, for driver pulses having a FWHM duration greater than five cycles, we find that the sampling response completely vanishes at the minima. This sampling technique allows for detection of higher harmonics of the driving signal regardless of the pulse duration, which originates from the fact that the individual peaks are deeply sub-cycle in duration[3].

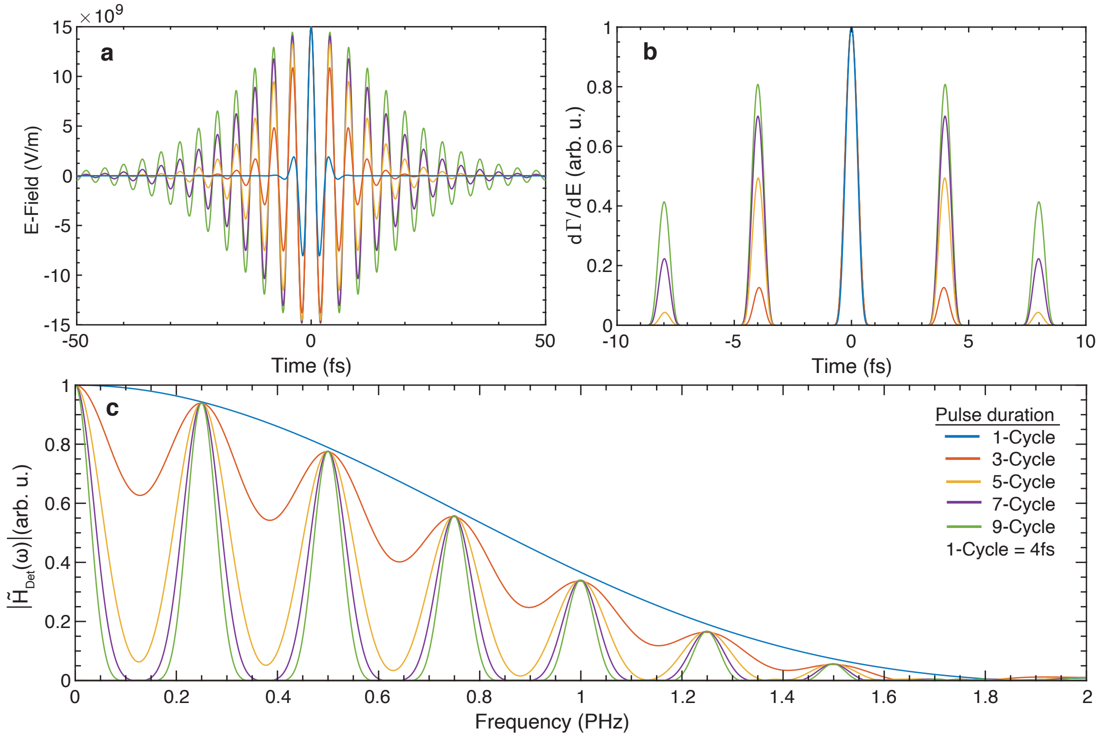

Figure S2. **Sampling bandwidth as a function of pulse duration. a,** Electric-field transients for near-infrared pulses with a FWHM duration of 1-, 3-, 5-, 7-, and 9-cycles and a central frequency of 250 THz. **b,** Calculation of $\frac{\mathrm{d}\Gamma}{\mathrm{d}E}\big|_{E_\mathrm{D}(t)}$ for the field transients shown in (A) and assuming $F_t = 78.7$ V nm^{-1} as the characteristic tunneling field. **c,** Fourier transform of $\frac{\mathrm{d}\Gamma}{\mathrm{d}E}\big|_{E_\mathrm{D}(t)}$ showing the accessible sampling bandwidth provided by the field transients shown in **a**.

S3. Carrier-Envelope Phase Discussion

The carrier-envelope phase (CEP) of a few-cycle pulse plays a significant role in strong-field physics and heavily influences the electron emission characteristics from resonant nanoantenna devices. In this section we discuss the role of the driving waveform's CEP in the sampling process. For simplicity in this section we will be discussing the field driving the emission at a surface, $E_\mathrm{D}(t)$.

For our analysis, we calculated the complex sampling response $\tilde{H}_\mathrm{Det}(\omega)$ assuming a sech^2 driving pulse with a central frequency of 250 THz and a pulse duration of 10 fs (∼2.5 cycle), as given by the output of the laser used to experimentally verify device performance. As in Sec. S1, the incident electric field was taken to be 15 GV m^{-1}. The results are plotted in Fig. S3a for various CEP values of the driving pulse. The small signal gain $\frac{\mathrm{d}\Gamma}{\mathrm{d}E}\big|_{E_\mathrm{D}(t)}$ was calculated by assuming Fowler-Nordheim tunnel emission with a characteristic tunneling field of $F_t = 78.7$ V nm^{-1} and is plotted in Fig. S3b. In Fig. S3c the complex sampling response

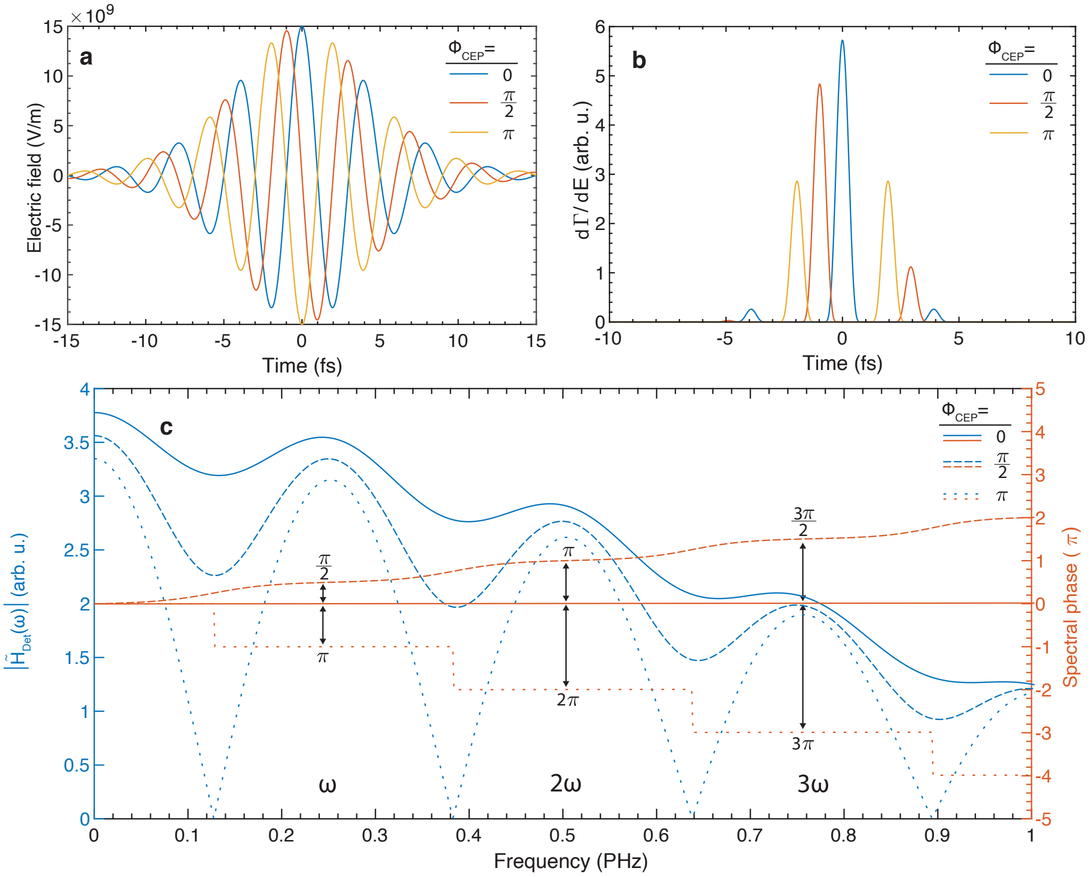

Figure S3. **Sampling response as a function of CEP. a,** Calculated sech^2 pulse centered at 250 THz with a pulse duration of 10 fs (2.5 cycles), a peak electric field of 15 GV m^{-1}, and a $\Phi_{\mathrm{CEP}} = 0,\ \frac{\pi}{2},\ \pi$. **b,** The small signal gain $\frac{\mathrm{d}\Gamma}{\mathrm{d}E}\big|_{E_{\mathrm{D}}(t)}$ is calculated by assuming Fowler-Nordheim tunneling emission with a characteristic tunneling field of $F_t =$ 78.7 V nm^{-1}. The electric-field transients used here correspond to **a**. **c,** The spectral amplitude and phase of the complex sampling response of $\tilde{H}_{\mathrm{Det}}(\omega)$ as a function of frequency. Calculated for $\Phi_{\mathrm{CEP}} = 0,\ \frac{\pi}{2}, \pi$.

$\tilde{H}_{\mathrm{Det}}(\omega)$ derived from $\frac{\mathrm{d}\Gamma}{\mathrm{d}E}\big|_{E_{\mathrm{D}}(t)}$ is shown.

The CEP, Φ_{CEP}, of the driving pulse dictates the amplitude of the modulation of $\tilde{H}_{\mathrm{Det}}(\omega)$. For the driver pulse duration modeled in Fig. S3a, a cosine shaped pulse ($\Phi_{\mathrm{CEP}} = 0$) exhibits minimal modulation of the sampling bandwidth, which corresponds to an isolated electron burst with small satellites in the time-domain if the pulse is sufficiently short (see Fig. S2b). A CEP of $\Phi_{\mathrm{CEP}} = \pi$ corresponds to a negative cosine shaped pulse, which corresponds to two electron bursts of equal height, resulting in the sharp minima in the sampling bandwidth as shown in Fig. S3c (dotted traces). More importantly, with an adequately short driving pulse, it is possible to choose an appropriate Φ_{CEP} value such that only one electron burst dominates the field emission process, resulting in a smooth, unmodulated $\tilde{H}_{\mathrm{Det}}(\omega)$ from DC to 1 PHz, as shown in Fig. S2c. Nevertheless independently of Φ_{CEP} a full octave of spectrum can still be sampled with distortion due to $\tilde{H}_{\mathrm{Det}}$.

Another important characteristic of the sampling process to consider is the absolute phase of the sampled output. When $\Phi_{\mathrm{CEP}} = 0$, a dominant electron burst exists in the time domain and the absolute phase of the signal pulse will be transferred to the sampled output, as $\tilde{H}_{\mathrm{Det}}(\omega)$ will be a purely real function (see Fig. S3c). For comparison, if $\Phi_{\mathrm{CEP}} \neq 0$ the spectral phase of $\tilde{H}_{\mathrm{Det}}(\omega)$ is not flat. As shown in Fig. S3, this phase resembles a stair function with plateaus of flat phase around the central frequency ω_0 and its harmonics. Looking closely at Fig. S3, we see that we can write the spectral phase at the nth harmonic as $\angle\tilde{H}_{\mathrm{Det}}(n\omega) = n\cdot\Phi_{\mathrm{CEP}}$ for $n \varepsilon \mathbb{N}$. With these spectral phase behaviors, we then see that the constant phase component of the sampled output becomes the difference between that of the sampling pulse, $n\cdot\Phi_{\mathrm{CEP}}$, and that of the signal, Φ_{S}. Therefore, the constant, or absolute, phase of the sampled output can be written $\Phi_{\mathrm{S}} - n\cdot\Phi_{\mathrm{CEP}}$. In the case where the driving pulse, E_{D}, and the signal pulse, E_{S}, originate from the same laser source, they will share a common Φ_{CEP}, and in this case, the absolute phase of the sampled pulse will therefore be zero. Importantly, we should note that this result is independent of Φ_{CEP}, and even laser sources with a carrier envelope offset $f_{\mathrm{CEO}} \neq 0$ can be used for sampling. Lastly, we should additionally note that in stark contrast to other phase-sensitive techniques, like homo- and hetero-dyne detection, the absolute phase of E_{D} can be derived unambiguously *in situ* from the field emission current generated by E_{D} in our devices, as demonstrated in [1, 5].

S4. Field-Sampling Measurements with 200 nm Devices

Our technique was also tested using devices consisting of triangular antennas with a 200 nm height. These devices were designed to be off-resonant with the laser pulse and were fabricated on a separate chip from the 240 nm antenna. Fig. S4 presents the acquired cross-correlation trace (blue) for these devices. For each data set, 47 scans of 5 seconds acquisition time over the 100 fs time window were performed. Post-processing was done in Matlab. Each data set was Fourier transformed and windowed from 150 THz to 350 THz with a tukey-window (steepness of $\alpha = 0.2$). The resulting output was averaged in the time-domain.

We find good agreement between the measured trace (blue) to the simulated local signal field, $E_{\mathrm{S}}^{(\mathrm{L})}(t)$ (red). We note that both the measurement and simulated local signal fields are both slightly shorter than the calculated laser output (yellow). The reason for this is apparent when examining the pulses in the frequency

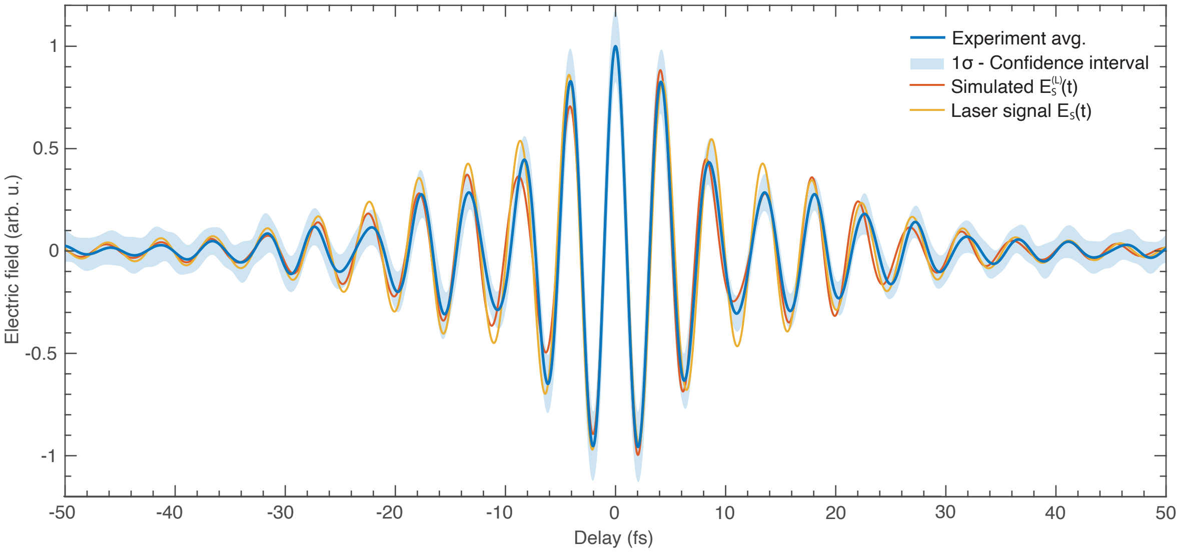

Figure S4. **Experimental field sampling results using 200 nm devices.** Time-domain results for 200 nm devices comparing measured (blue) and simulated near-fields ($E_{\mathrm{S}}^{(\mathrm{L})}(t)$, red) to the calculated incident laser signal ($E_{\mathrm{S}}(t)$, yellow). Here, negative delays indicate the driver pulse arrives before the signal pulse. The 200 nm device is designed to be off-resonant with the laser pulse and the measured trace yields good agreement to the calculated laser output. The 1σ-confidence interval is shown as a blue shaded ribbon centered at the average value (blue solid line) retrieved from 47 scans.

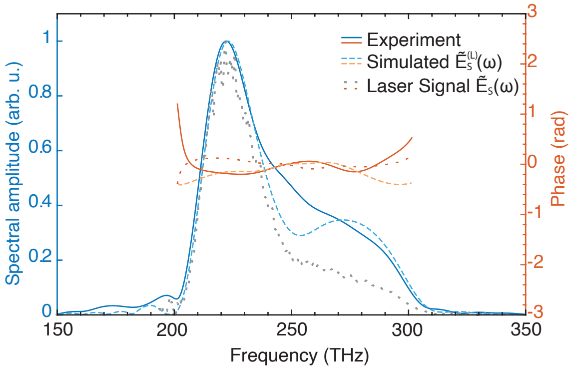

Figure S5. **Frequency-domain analysis of 200 nm device results.** Frequency-domain analysis comparing measured (solid) and simulated ($\tilde{E}_{\mathrm{S}}^{(\mathrm{L})}(\omega)$, dashed) near-fields for 200 nm devices to the calculated incident laser signal ($\tilde{E}_{\mathrm{S}}(\omega)$, dotted). The 200 nm device is designed to be off-resonant with the laser pulse, thus the measured and simulated spectrum only show a single spectral peak corresponding with that of the laser spectrum at $\approx$ 220 THz.

domain as shown in Fig. S5. While the main spectral peak at $\approx$ 220 THz agrees with the measured laser spectrum ($\tilde{E}_{\mathrm{S}}(\omega)$, gray dotted curve) and the expected antenna response ($\tilde{E}_{\mathrm{S}}^{(\mathrm{L})}(\omega)$, light blue dashed curve), both the simulated and experimental local signal field spectra exhibit an enhanced shoulder out to 300 THz relative to the measured laser output spectrum (solid blue curve). This is due to the plasmonic resonance which enhances these higher frequency components, resulting in a shorter time domain response of the local fields relative to the incident fields after interaction with the antenna.

S5. Data Processing and Error Analysis

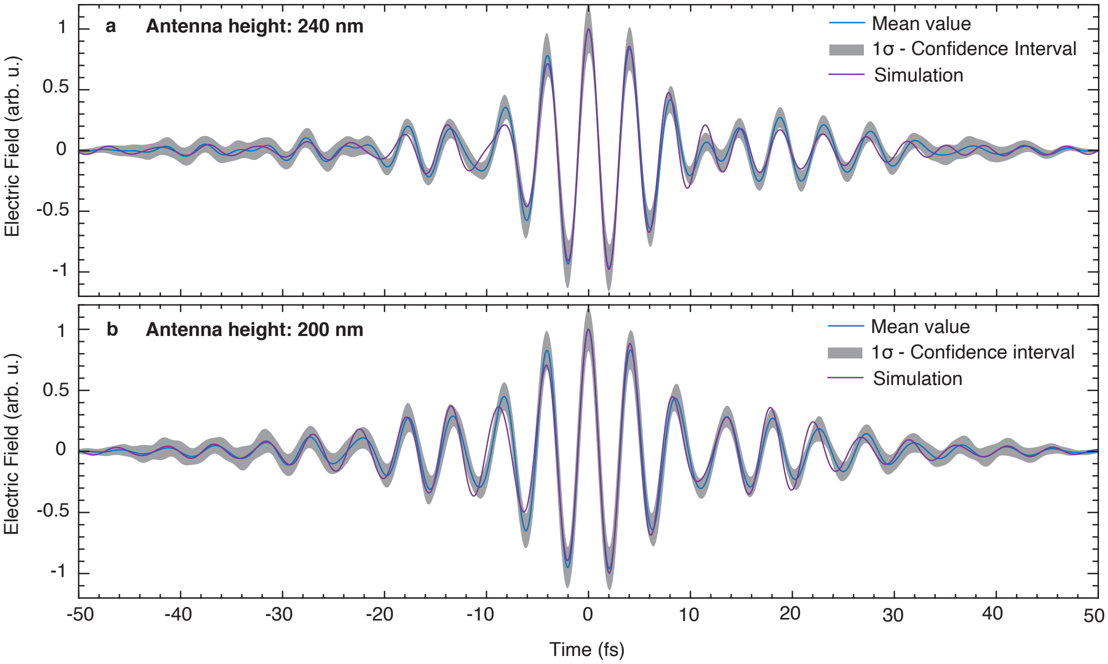

Figure S6. **Mean value and 1σ-confidence interval** Time-domain measurement and simulation for **a** 240 nm devices (Fig. 3, main text), and **b** 200 nm devices (Fig. S4). The blue curves shows the mean value for every electric field/time coordinate over all individual scans. The grey ribbon shows the 1σ-confidence interval for the respective coordinate. For comparison, the simulated electric field is shown in purple.

To determine the error in our measurement, we took the Fourier transform of the each of the $\sim$50 individual data sets and applied a tukey-window in the frequency-domain with a steepness of $\alpha = 0.2$ from 150 THz to 350 THz. The windowed data sets were then back transformed into the time-domain and averaged for each time coordinate over all data sets. To determine the 1σ-confidence interval the standard deviation was calculated for each time coordinate over all data sets. The result is shown in Fig. S6 and compared to the respective simulation shown in Fig. 3 (main text) for the 240 nm devices and Fig. S4 for the 200 nm devices.

S6. Source Spectral Phase Measurements

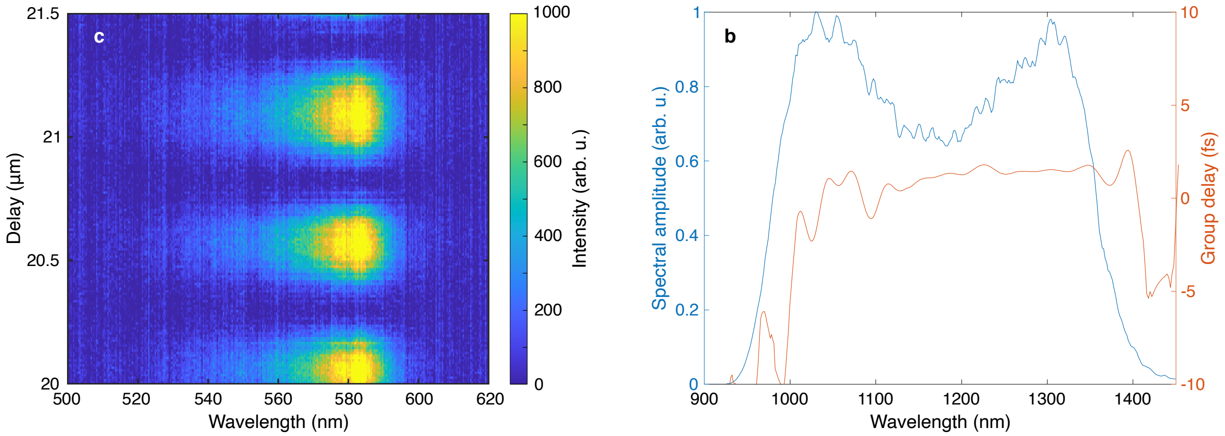

Figure S7. **Source spectral phase characterization using 2DSI. a,** Raw 2DSI spectrogram of the source in the experiment conditions. **b,** Retrieved group delay (red) and laser spectrum (blue). The optimized values of shear frequency and upconversion wavelength are $f_{\text{shear}} = 5.5$ THz and $\lambda_{\text{up}} = 1050$ nm.

In order to characterize the spectral phase of our supercontinuum source we performed two-dimensional spectral shearing interferometry (2DSI) measurements[6]. Two spectrograms were obtained for the measurement: the first with the laser in similar conditions to that of the experiment, and the second with an added 1.5 mm fused silica window placed in the beam path. The spectrogram of the source in the experimental conditions is shown in Fig. S7a. The second spectrogram taken with an additional propagation through 1.5 mm fused silica was used to calibrate the shear frequency f_{shear} and upconversion wavelength λ_{up} needed for group delay retrieval from the 2DSI measurement. Using an optimization routine, we found the values for f_{shear} and λ_{up} that resulted in the minimum error between the group delay difference measured with and without the fused silica using 2DSI and that predicted using the known optical properties of fused silica. The resulting retrieved group delay and the spectrum of our laser source are reported in Fig. S7b.

References

[1] T. Rybka, M. Ludwig, M. F. Schmalz, V. Knittel, D. Brida, and A. Leitenstorfer, "Sub-cycle optical phase control of nanotunnelling in the single-electron regime", Nat. Photon. **10**, 667–670 (2016).

[2] W. P. Putnam, R. G. Hobbs, P. D. Keathley, K. K. Berggren, and F. X. Kärtner, "Optical-field-controlled photoemission from plasmonic nanoparticles", Nat. Phys. **13**, 335–339 (2017).

[3] P. D. Keathley, W. P. Putnam, P. Vasireddy, R. G. Hobbs, Y. Yang, K. K. Berggren, and F. X. Kärtner, "Vanishing carrier-envelope-phase-sensitive response in optical-field photoemission from plasmonic nanoantennas", Nat. Phys. **15**, 1128 (2019).

[4] M. Ludwig, G. Aguirregabiria, F. Ritzkowsky, T. Rybka, D. C. Marinica, J. Aizpurua, A. G. Borisov, A. Leitenstorfer, and D. Brida, "Sub-femtosecond electron transport in a nanoscale gap", Nat. Phys. **16**, 341–345 (2020).

[5] Y. Yang, M. Turchetti, P. Vasireddy, W. P. Putnam, O. Karnbach, A. Nardi, F. X. Kärtner, K. K. Berggren, and P. D. Keathley, "Light Phase Detection with On-Chip Petahertz Electronic Networks", Nat. Commun. **11**, 3407 (2020).

[6] J. R. Birge, R. Ell, and F. X. Kärtner, "Two-dimensional spectral shearing interferometry for few-cycle pulse characterization", Opt. Lett. **31**, 2063 (2006).